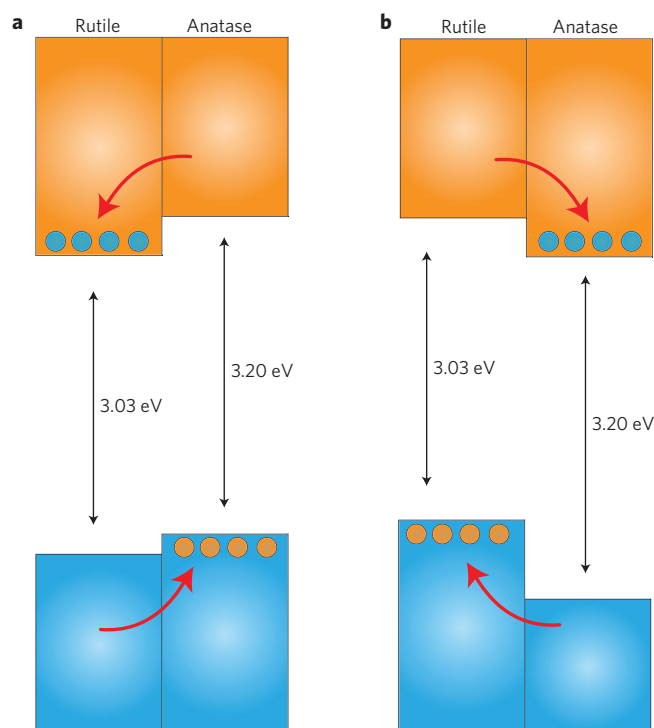# Band alignment of rutile and anatase TiO$_2$

David O. Scanlon[1]*, Charles W. Dunnill[2], John Buckeridge[1]*, Stephen A. Shevlin[1], Andrew J. Logsdail[1], Scott M. Woodley[1], C. Richard A. Catlow[1], Michael. J. Powell[2], Robert G. Palgrave[2], Ivan P. Parkin[2], Graeme W. Watson[3], Thomas W. Keal[4], Paul Sherwood[4], Aron Walsh[5] and Alexey A. Sokol[1]

The most widely used oxide for photocatalytic applications owing to its low cost and high activity is TiO$_2$. The discovery of the photolysis of water on the surface of TiO$_2$ in 1972[1] launched four decades of intensive research into the underlying chemical and physical processes involved[2-5]. Despite much collected evidence, a thoroughly convincing explanation of why mixed-phase samples of anatase and rutile outperform the individual polymorphs has remained elusive[6]. One long-standing controversy is the energetic alignment of the band edges of the rutile and anatase polymorphs of TiO$_2$ (ref. 7). We demonstrate, through a combination of state-of-the-art materials simulation techniques and X-ray photoemission experiments, that a type-II, staggered, band alignment of ∼0.4 eV exists between anatase and rutile with anatase possessing the higher electron affinity, or work function. Our results help to explain the robust separation of photoexcited charge carriers between the two phases and highlight a route to improved photocatalysts.

A general consensus places the bandgaps of rutile and anatase TiO$_2$ at 3.03 and 3.20 eV, respectively. In 1996, electrochemical impedance analysis established that the flatband potential of anatase is ∼0.2 eV more negative than that of rutile, indicating that the conduction band of anatase lies 0.2 eV above that of rutile[8]. This band alignment, illustrated in Fig. 1a, would favour the transfer of photogenerated electrons from anatase to rutile, and the transfer of holes from rutile to anatase at a clean interface (although the valence band positions in this alignment are very similar) and was supported by several experiments[9-11]. Alternatively, recent photoemission measurements have reported that the work function of rutile is 0.2 eV lower than that of anatase, placing the conduction band of anatase 0.2 eV below that of rutile[12] (Fig. 1b).

Electron paramagnetic resonance experiments focusing on mixed rutile/anatase samples have demonstrated that electrons flow from rutile into anatase, with holes moving in the opposite direction[13-16]. These studies have provided information on the interface (for example, a newly discovered interfacial trapping site, lattice and surface electron trapping sites, and surface hole trapping sites) and on recombination in these mixed samples[14,15]. The fundamental band alignment between anatase and rutile, which is necessarily the driving force for the kinetics of both ionic and electronic charge carriers, however, is still not understood. The intrinsic band alignment will always act as the boundary conditions imposed on a particular interface, and will be a dominant factor in any photocatalytic activity.


Figure 1 | Two proposed valence and conduction band alignment mechanisms for the anatase/rutile interface. a, Type-II (rutile). **b**, Type-II (anatase). The present study supports model **b**. Red arrows indicate the flow of electrons (holes) in the conduction band (valence band). Blue and orange dots represent electrons and holes, respectively.

To understand the band alignment of anatase and rutile TiO$_2$, we have carried out three separate computational analyses on both polymorphs: electronic structure of bulk crystals; electrostatic analysis of the Ti and O environments; absolute vacuum alignment from embedded crystals.

First, periodic hybrid density functional theory calculations with a plane-wave basis set (the Vienna *ab initio* simulation package code[17]) were performed to understand the electronic structure and nature of the band edge wavefunctions. We employed a screened non-local exchange-correlation density functional (HSE06)[18], with full details provided in the Supplementary Information. In Fig. 2,

[1]University College London, Kathleen Lonsdale Materials Chemistry, 20 Gordon Street, London, WC1H OAJ, UK, [2]Centre for Materials Research, Department of Chemistry, University College London, 20 Gordon Street, London, WC1H 0AJ, UK, [3]School of Chemistry and CRANN, Trinity College Dublin, Dublin 2, Ireland, [4]Scientific Computing Department, STFC, Daresbury Laboratory, Daresbury, Warrington, WA4 4AD, UK, [5]Centre for Sustainable Chemical Technologies and Department of Chemistry, University of Bath, Claverton Down, Bath BA2 7AY, UK. *e-mail: d.scanlon@ucl.ac.uk; j.buckeridge@ucl.ac.uk
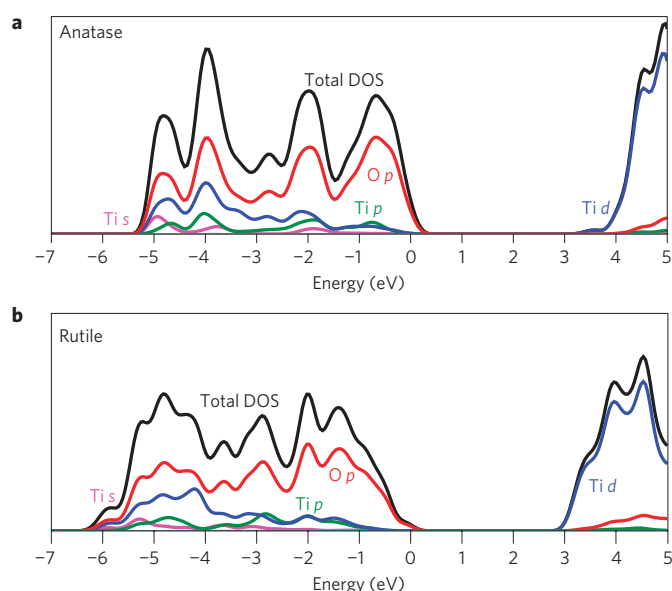
Figure 2 | Electronic structure of anatase and rutile TiO₂. a,b, Comparison of the total and ion-decomposed electronic density of states of anatase (**a**) and rutile (**b**) TiO₂ calculated using the HSE06 hybrid density functional.

we show the electronic density of states for rutile and anatase. The valence band edge of both materials is dominated by O 2p, and the conduction band edge is formed from Ti 3d. The widths of the upper valence bands are similar in each phase, which indicates that neither anatase nor rutile experience a significant chemical broadening that could offset the valence band edge position. Therefore, the position of the conduction and valence bands of ionic materials such as TiO₂ is determined by the onsite electrostatic potential and the optical dielectric response.

The analysis in Fig. 2 illustrates that excess electrons in these materials will be centred on the d states of cations, whereas electron holes are centred on 2p states of oxygen, which is consistent with electron paramagnetic resonance data. We have calculated the local Madelung potentials[19] of Ti and O in both anatase and rutile using the polarizable shell model[20,21], fitted to reproduce accurately the high-frequency dielectric constants of TiO₂. Note that negatively charged electrons have a lower energy the higher the Madelung potential (cation sites have a negative potential) whereas the energy to create a positive hole is lower, the lower the Madelung energy (anion sites have a positive potential). This analysis indicates that the Madelung potential of Ti in anatase (-45.025 V) is 0.17 eV higher than the potential of Ti in rutile (-45.199 V). The offset is in excellent agreement with recent photoemission measurements. Similarly, the Madelung potential of O in anatase (26.232 V) is higher than the Madelung potential of O in rutile (25.767 V), placing the valence band of rutile 0.47 eV above the valence band of anatase, in agreement with the alignment shown in Fig. 1b. In support of this fundamental argument, we have calculated energies of charge carriers propagating at the band edges using the Mott–Littleton defect approach, which includes the high-frequency dielectric response of the material[22]. The calculated difference in carrier energies between the two materials strongly corroborates the band alignment put forward above. In particular, for the electrons at the bottom of the conduction band we obtain a 0.24 eV shift downwards of the anatase conduction band relative to rutile, whereas for the hole carrier we find the valence band of rutile to be 0.39 eV higher in energy than that of anatase. Both the Madelung-potential-based argument and 'defect' models predicted correctly the bandgap opening of ~0.2 eV in anatase relative to rutile.

Last, we have calculated the ionization potentials of both polymorphs relative to the vacuum level using a hybrid quantum-mechanical/molecular-mechanical[23] (QM/MM) embedding technique as implemented in the ChemShell code[24]. In this approach, a part of the crystal is represented by a molecular cluster (treated at a QM level of theory) embedded in an external potential, which represents the system remainder (treated at an MM level of theory), as illustrated in Fig. 3a. Exploiting the accurate account of electronic polarization by the MM model introduced above, we are able to calculate the system response to ionization, on which all electronic degrees of freedom are fully relaxed while keeping the nuclei frozen. The ionization potential is calculated by taking the energy difference between a (electronically) relaxed system in the neutral and positive charge states (see Supplementary Information for details). We have calculated the ionization potential of both rutile and anatase for a series of QM cluster sizes (from ~50 atoms to ~80 atoms), using a well-converged basis set. The model consistently predicts an offset of ~0.47 eV between rutile and anatase, with the rutile valence band higher in energy than anatase, as indicated in Fig. 3b.

The calculations place the ionization potential of rutile at 7.83 eV, with the ionization potential of anatase at 8.30 eV. Previous studies have assumed that the ionization potential of rutile is 7.1 eV (ref. 25), although this is inferred from the conduction band position taken from ref. 8. The accuracy of our approach is supported by comparison with a recent X-ray photoelectron spectroscopy (XPS) alignment of rutile TiO₂ with ZnO, which found that the valence band of rutile is 0.14 eV lower[22]. The experimental ionization potential of ZnO is known to be 7.82 eV, (ref. 26) and is well described by the QM/MM approach (7.71 eV; ref. 27). Indeed, the offset between the calculated ionization potentials for rutile and ZnO (0.12 eV) is in excellent agreement with the experimental offset of 0.14 eV. In addition, our calculated electron affinities for rutile (4.8 eV) and anatase (5.1 eV) are in good agreement with those experimentally measured, that is 4.9 eV for rutile, 5.1 eV for anatase[12]. The effective bandgap for a clean rutile/anatase heterojunction should therefore be lowered to ~2.78 eV, a significant redshift from the isolated phases.

To test the model band alignment, we have fabricated high-quality anatase–rutile junctions. Nanoparticulate heterostructures were achieved using a sol–gel approach from a titanium n-butoxide precursor. A uniform interface was formed by dip-coating successive layers onto a NaCl substrate; first rutile (700 °C anneal) and later anatase (500 °C anneal). The original substrate was then dissolved in water, leaving a freestanding rutile–anatase bilayer. For full details of the synthesis and characterization of these materials, see the Supplementary Information. High-resolution XPS was used to determine the band offsets based on core level shifts, following the method of refs 28–30. The binding energy difference between the Ti 2$p_{3/2}$ core line and the valence band was first determined in samples of phase-pure anatase and rutile. In each case the core lines for the phase-pure samples were fitted with a Gaussian–Lorentzian function. These same functions were used to peak fit the Ti 2$p_{3/2}$ spectrum obtained from the composite particles, and so obtain the binding energies (Fig. 3c), and hence the valence band offsets (Fig. 3d). To aid this peak fitting, samples were produced with a 2:1, 1:1 and 1:2 ratio of rutile to anatase. Full details of this procedure are given in the Supplementary Information. The anatase valence band was found to be at 0.39 ± 0.02 eV higher binding energy than rutile for the composite samples. These results were obtained independently of the computational analysis.

In conclusion, we have combined theory and experiment to revise the understanding of the band alignment between rutile and anatase. A consistent picture emerged, where in contrast to the widely accepted alignment model, we demonstrate that the electron affinity of anatase is higher than rutile. Photogenerated

799
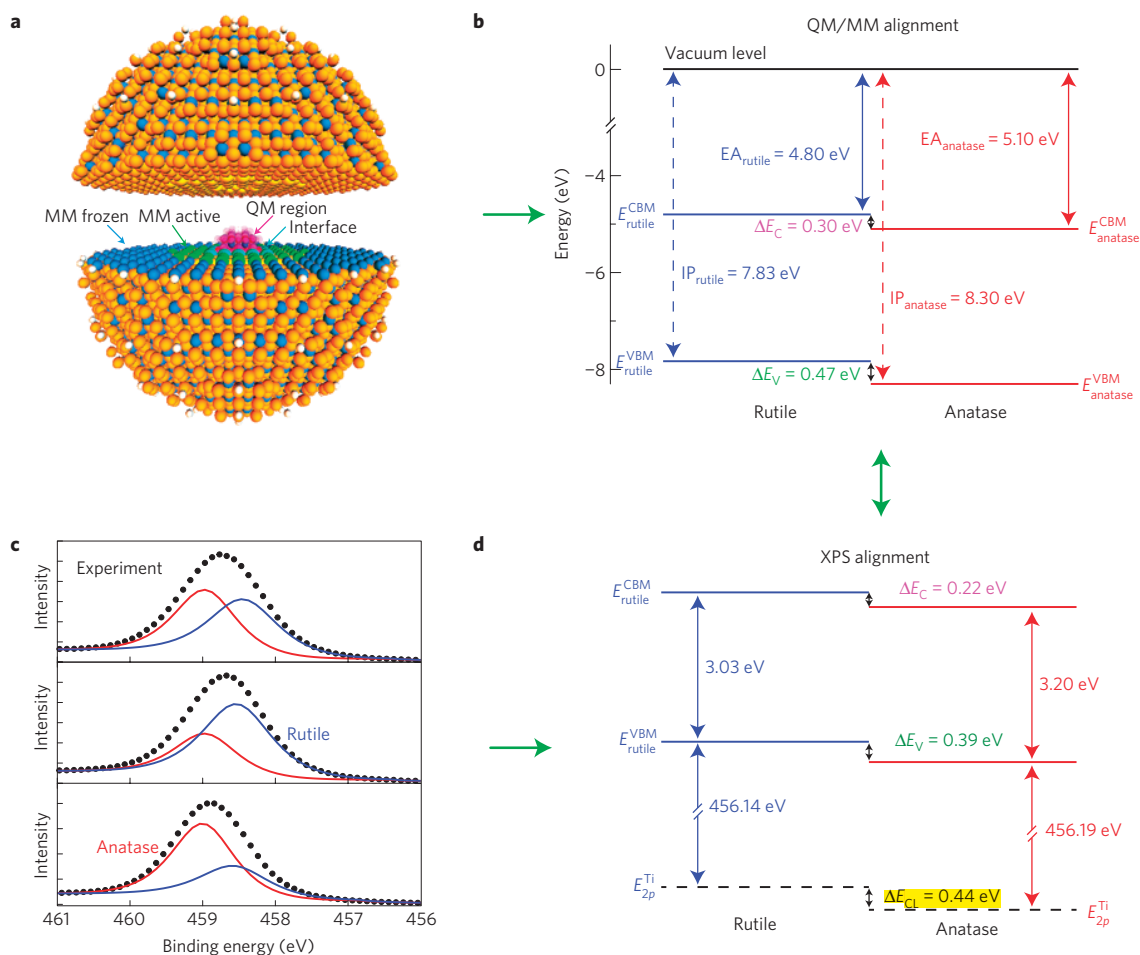
Figure 3 | Band alignment between rutile and anatase from XPS and QM/MM. a, Graphic of the hybrid QM/MM cluster used for rutile in the positive charge state. The cluster is divided into hemispheres to highlight the different regions in the model. Hole density iso-surfaces are shown (semi-transparent purple) in the QM region. **b,** Schematic of the QM/MM alignment of rutile and anatase TiO_2. IP and EA denote ionization potential and electron affinity, respectively. The electron affinity is calculated by adding the experimental bandgaps to the calculated ionization potentials. ΔE_V and ΔE_C are the valence band offsets and conduction band offsets, respectively and E^{CBM} and E^{VBM} denote the positions of the conduction band and valence band respectively. **c,** Ti $2p_{3/2}$ spectra are taken from two phase composite particles with rutile to anatase ratios of 1:1 (top) and 2:1 (middle) and 1:2 (bottom). Experimental data, shown as black dots, are fitted with the peak shapes derived from phase-pure anatase (red) and rutile (blue). **d,** Schematic of the XPS alignment between rutile and anatase. ΔE_{CL} is the core level offset between the Ti $2p_{3/2}$ core levels.

conduction electrons will flow from rutile to anatase. A type II band alignment of $\sim$0.4 eV is present, significantly lowering the effective bandgap of composite materials, and facilitating efficient electron–hole separation. This alignment is the likely driving force for the increased photoactivity of anatase–rutile composite materials over their individual counterparts.

Despite having the same chemical composition, the differences in the coordination environments, and hence chemical bonding, of rutile- and anatase- structured TiO_2 result in very different ionization potentials and electron affinities. Exploitation of the relationship between the electron chemical potentials and crystal structure could be used to design new photoactive materials and composites, especially where there are a number of accessible polytypes or interfacial morphologies. This should lead towards both higher efficiencies in the photolysis of water and more robust electron–hole separation in dye-sensitized solar cells.

References

1. Fujishima, A. & Honda, K. Electrochemical photolysis of water at a semiconductor electrode. *Nature* **238,** 37–38 (1972).
2. Dunnill, C. W. *et al.* Nanoparticulate silver coated-titania thin films-Photo-oxidative destruction of stearic acid under different light sources and antimicrobial effects under hospital lighting conditions. *J. Photochem. Photobiol. A* **220,** 113–123 (2011).
3. Gratzel, M. Photoelectrochemical cells. *Nature* **414,** 338–344 (2001).
4. Khan, S. U. M., Al-Shahry, M. & Ingler, W. B. Efficient photochemical water splitting by a chemically modified n-TiO₂. *Science* **297,** 2243–2245 (2002).
5. Yang, H. G. *et al.* Anatase TiO₂ single crystals with a large percentage of reactive facets. *Nature* **453,** 638–641 (2008).
6. Li, G. H. & Gray, K. A. The solid-solid interface: Explaining the high and unique photocatalytic reactivity of TiO₂-based nanocomposite materials. *Chem. Phys.* **339,** 173–187 (2007).
7. Deak, P., Aradi, B. & Frauenheim, T. Band lineup and charge carrier separation in mixed rutile-anatase systems. *J. Phys. Chem. C* **115,** 3443–3446 (2011).
8. Kavan, L., Gratzel, M., Gilbert, S. E., Klemenz, C. & Scheel, H. J. Electrochemical and photoelectrochemical investigation of single-crystal anatase. *J. Am. Chem. Soc.* **118,** 6716–6723 (1996).
9. Kawahara, T. *et al.* A patterned TiO₂(anatase)/TiO₂(rutile) bilayer-type photocatalyst: Effect of the anatase/rutile junction on the photocatalytic activity. *Angew. Chem. Int. Ed.* **41,** 2811–2813 (2002).
10. Miyagi, T., Kamei, M., Mitsuhashi, T., Ishigaki, T. & Yamazaki, A. Charge separation at the rutile/anatase interface: A dominant factor of photocatalytic activity. *Chem. Phys. Lett.* **390,** 399–402 (2004).
11. Nakajima, H., Mori, T., Shen, Q. & Toyoda, T. Photoluminescence study of mixtures of anatase and rutile TiO₂ nanoparticles: Influence of charge transfer between the nanoparticles on their photo luminescence excitation bands. *Chem. Phys. Lett.* **409,** 81–84 (2005).

12. Xiong, G. *et al.* Photoemission electron microscopy of TiO_2 anatase films embedded with rutile nanocrystals. *Adv. Funct. Mater* **17**, 2133–2138 (2007).
13. Hurum, D. C. *et al.* Probing reaction mechanisms in mixed phase TiO_2 by EPR. *J. Electron Spectrosc.* **150**, 155–163 (2006).
14. Hurum, D. C., Agrios, A. G., Gray, K. A., Rajh, T. & Thurnauer, M. C. Explaining the enhanced photocatalytic activity of Degussa P25 mixed-phase TiO_2 using EPR. *J. Phys. Chem. B* **107**, 4545–4549 (2003).
15. Hurum, D. C., Gray, K. A., Rajh, T. & Thurnauer, M. C. Recombination pathways in the Degussa P25 formulation of TiO_2: Surface versus lattice mechanisms. *J. Phys. Chem. B* **109**, 977–980 (2005).
16. Leytner, S. & Hupp, J. T. Evaluation of the energetics of electron trap states at the nanocrystalline titanium dioxide/aqueous solution interface via time-resolved photoacoustic spectroscopy. *Chem. Phys. Lett.* **330**, 231–236 (2000).
17. Kresse, G. & Hafner, J. *Ab-initio* molecular-dynamics simulation of the liquid-metal amorphous-semiconductor transition in germanium. *Phys. Rev. B* **49**, 14251–14269 (1994).
18. Krukau, A. V., Vydrov, O. A., Izmaylov, A. F. & Scuseria, G. E. Influence of the exchange screening parameter on the performance of screened hybrid functionals. *J. Chem. Phys.* **125**, 224106 (2006).
19. Madelung, E. The electric field in systems of regularly arranged point charges. *Phys. Z* **19**, 524–533 (1918).
20. Dick, B. G. & Overhauser, A. W. Theory of the dielectric constants of alkali halide crystals. *Phys. Rev.* **112**, 90–103 (1958).
21. Catlow, C. R. A. *et al.* Advances in computational studies of energy materials. *Philos. Trans. R. Soc. A-Math. Phys. Eng. Sci.* **368**, 3379–3456 (2010).
22. Wang, J. *et al.* Measurement of wurtzite ZnO/rutile TiO_2 heterojunction band offsets by X-ray photoelectron spectroscopy. *Appl. Phys. A* **103**, 1099–1103 (2011).
23. Sokol, A. A., Bromley, S. T., French, S. A., Catlow, C. R. A. & Sherwood, P. Hybrid QM/MM embedding approach for the treatment of localized surface states in ionic materials. *Int. J. Quantum Chem.* **99**, 695–712 (2004).
24. Sherwood, P. *et al.* QUASI: A general purpose implementation of the QM/MM approach and its application to problems in catalysis. *J. Mol. Struct.-Theochem.* **632**, 1–28 (2003).
25. Cheng, J. & Sprik, M. Aligning electronic energy levels at the TiO_2/H_2O interface. *Phys. Rev. B* **82**, 081406 (2010).
26. Swank, R. K. Surface properties of 2–6 compounds. *Phys. Rev.* **153**, 844–849 (1967).
27. Sokol, A. A. *et al.* Point defects in ZnO. *Faraday Discuss.* **134**, 267–282 (2007).
28. Grant, R. W., Kraut, E. A., Kowalczyk, S. P. & Waldrop, J. R. Measurement of potential at semiconductor interfaces by electron-spectroscopy. *J. Vac. Sci. Technol. B* **1**, 320–327 (1983).
29. Kraut, E. A., Grant, R. W., Waldrop, J. R. & Kowalczyk, S. P. Semiconductor core-level to valence-band maximum binding-energy differences—precise determination by X-ray photoelectron-spectroscopy. *Phys. Rev. B* **28**, 1965–1977 (1983).
30. Waldrop, J. R., Kowalczyk, S. P., Grant, R. W., Kraut, E. A. & Miller, D. L. XPS measurement of GaAs-AlAs heterojunction band discontinuities—growth sequence dependence. *J. Vac. Sci. Technol.* **19**, 573–575 (1981).

Author contributions

D.O.S. wrote the manuscript with input from A.W. and A.A.S. D.O.S. and A.A.S. designed the computational experiments. C.W.D., M.J.P., R.G.P. and I.P.P. designed and performed the sample growth and XPS experiments. A.A.S., S.M.W. and C.R.A.C. calculated and analysed the band offsets using the method of interatomic potentials, D.O.S., S.A.S. and G.W.W. performed and analysed the periodic DFT calculations, and J.B., A.J.L., A.A.S., T.W.K. and P.S. developed, performed and analysed the QM/MM alignments. All authors contributed to the scientific discussion and edited the manuscript.

Additional information

Supplementary information is available in the online version of the paper. Reprints and permissions information is available online at www.nature.com/reprints. Correspondence and requests for materials should be addressed to D.O.S. or J.B.

Competing financial interests

The authors declare no competing financial interests.